Cryo-EM structure of the fully-loaded asymmetric anthrax lethal toxin in its heptameric pre-pore state

Claudia Antoni[1,*], Dennis Quentin[1,*], Alexander E. Lang[2], Klaus Aktories[2], Christos Gatsogiannis [1], Stefan Raunser[1†]

[1]Department of Structural Biochemistry, Max Planck Institute of Molecular Physiology, 44227 Dortmund, Germany

[2]Institute of Experimental and Clinical Pharmacology and Toxicology, Faculty of Medicine, University of Freiburg, 79104 Freiburg, Germany

*These authors contributed equally

†Correspondence: stefan.raunser@mpi-dortmund.mpg.de

Abstract

Anthrax toxin is the major virulence factor secreted by *Bacillus anthracis*, causing high mortality in humans and other mammals. It consists of a membrane translocase, known as protective antigen (PA), that catalyzes the unfolding of its cytotoxic substrates lethal factor (LF) and edema factor (EF), followed by translocation into the host cell. Substrate recruitment to the heptameric PA pre-pore and subsequent translocation, however, are not well understood. Here, we report three high-resolution cryo-EM structures of the fully-loaded anthrax lethal toxin in its heptameric pre-pore state, which differ in the position and conformation of LFs. The structures reveal that three LFs interact with the heptameric PA and upon binding change their conformation to form a continuous chain of head-to-tail interactions. As a result of the underlying symmetry mismatch, one LF binding site in PA remains unoccupied. Whereas one LF directly interacts with a part of PA called α-clamp, the others do not interact with this region, indicating an intermediate state between toxin assembly and translocation. Interestingly, the interaction of the N-terminal domain with the α-clamp correlates with a higher flexibility in the C-terminal domain of the protein. Based on our data, we propose a model for toxin assembly, in which the order of LF binding determines which factor is translocated first.

Introduction

Anthrax is a life-threatening infectious disease that affects primarily livestock and wild animals, but can also cause high mortality in humans (1). During the early and late steps of infection with the Gram-positive bacterium *B. anthracis*, the tripartite anthrax toxin is secreted as major virulence factor in order to kill host immune cells such as macrophages or neutrophils (2,3). Like other AB-type toxins, it is composed of a surface binding/translocation moiety, the protective antigen (PA, 83 kDa), and two cytotoxic subunits, lethal factor (LF, 90 kDa) and edema factor (EF, 93 kDa) (4,5).

To execute their toxicity, both the zinc-dependent metalloproteinase LF and/or the adenylate cyclase EF need to enter the host cytoplasm (6,7). For that purpose, PA monomers first attach to the cell surface through binding to one of the two known membrane receptors, capillary morphogenesis gene 2 (CMG-2) and tumor endothelial marker 8 (TEM8) (8,9). After cleavage by furin-like proteases, the truncated 63 kDa-sized PA monomer oligomerizes either into homo-heptamers (PA_7) or homo-octamers (PA_8) (10-12). These ring-shaped oligomers, enriched in lipid raft regions, are in a pre-pore conformation as they do not penetrate the host membrane (13). Due to the enhanced stability of PA_8 under diverse physiological conditions, it is proposed that the octameric form could circulate in the blood to reach and exert toxicity even in distant tissues (14). This suggests that both oligomeric forms play an important role in intoxication, endowing *B. anthracis* with greater versatility against its host.

In the next step, the holotoxin is assembled by recruiting LFs/EFs. While PA_8 can bind up to four factors, only three of them can simultaneously bind to PA_7. Both enzymatic substrates bind to the upper rim of the PA oligomer via their N-terminal domains in a competitive manner (15). Loaded complexes are then endocytosed (16,17), followed by a conformational change from the pre-pore to pore state which is triggered by the low pH in the endosome (18). The central feature of the pore state is an 18 nm long 14-stranded β-barrel that spans the endosomal membrane with its narrowest point in the channel lumen being ~6 Å in width (19). To pass

through this hydrophobic restriction, called Φ-clamp, the substrate needs to be unfolded prior to translocation (20).

Structural and functional studies on the pre-pore PA octamer bound to four LFs revealed that an amphipathic cleft between two adjacent PA protomers, termed α-clamp by Krantz and coworkers, assist in the unfolding process (21). More specifically, the first α-helix and β-strand (α1-β1) of LF almost completely unfold and change their position respective to the rest of the protein when interacting with the α-clamp of the PA oligomer (21). After transition into the pore state, the unidirectional translocation of LF is driven by a proton-motive force, comprising the proton gradient between the two compartments and the membrane potential. It is thought that the acidic pH present in the endosome destabilizes the LF and thus promotes unfolding of its N-terminus (22). Ultimately, it is believed that the translocation follows a 'charge-dependent Brownian ratchet' mechanism (23). The required unfolding and refolding of translocated enzymes is facilitated *in vivo* by chaperones, but can occur *in vitro* without the need of accessory proteins (24,25).

Crystallographic studies provided us with structural insights pertinent to the molecular action of the anthrax toxin. This includes structures of the individual complex subunits such as LF, EF and the PA pre-pore in both, its heptameric and octameric form (12,26-29). The PA monomer was also co-crystallized with its receptor CMG-2, delineating the surface attachment to the host cell in molecular detail. More recently, the elusive pore state of PA_7 was determined by electron cryo-microscopy (cryo-EM) in which Jiang *et al*. made use of an elegant on-grid pore induction approach (30).

In contrast, high resolution information on holotoxin complexes is rather scarce. The only obtained crystallographic structure is the aforementioned PA_8 pre-pore in complex with four LFs (21). In this structure, however, the C-terminal domain of LF is absent. Unlike PA_8, loaded PA_7 was mainly studied by cryo-EM (31-35), presumably because its asymmetry impeded crystallization efforts. Earlier this year, the PA_7 pore state decorated with a single LF

molecule and with up to two EF molecules was determined, in which it was shown that EF undergoes a large conformational rearrangement as opposed to LF (36). However, cryo-EM studies of the loaded heptameric pre-pore were so far limited to a resolution of ~16 Å (31,32,34). In addition, the number of LFs bound to PA_7 varied between one and three in these structures.

Here, we present three cryo-EM structures of the fully loaded anthrax lethal toxin in the heptameric pre-pore state (PA_7LF_3), in which three LF molecules are bound to the rim of the PA_7 ring, forming a continuous chain of head-to-tail interactions. The position and conformation of the LFs, however, varies between the structures. Unexpectedly, only one of three LFs interacts with the α-clamp of PA, adopting the "open" conformation as reported in the PA_8LF_4 structure (21). Since we could neither observe a similar interaction for the other two LFs, nor them being in the "closed" conformation, we propose that they adopt an "intermediate" state between holotoxin assembly and translocation. Our findings allow us to propose a model for anthrax lethal toxin assembly, in which the LF translocation sequence is dictated by the order of LF binding.

Results

Structure of the fully-loaded anthrax lethal toxin in the heptameric pre-pore state

To ensure that our purified and reconstituted PA_7 complexes (Materials and Methods) are indeed intact, we tested their membrane insertion capacity by reconstituting them in liposomes or nanodiscs (Fig. S1). We then evaluated different molar ratios of LF:PA_7 and only obtained fully-loaded anthrax lethal toxin (PA_7LF_3) when using a 10:1 molar ratio as judged by size exclusion chromatography (Fig. S2A, B).

We then determined the structure of the PA_7LF_3 pre-pore complex by single particle cryo-EM to an average resolution of 3.5 Å. However, the densities corresponding to LF represented a mixture of assemblies and were partly unassignable (Fig. S3). This can be either due to the symmetry mismatch that emerges when three lethal factors bind simultaneously to PA_7 or to possible different conformations of the individual LFs bound to PA_7. To address these points, we established an image processing workflow that includes sequential 3-D classifications and rotation of classes (Fig. S3). This resulted in three reconstructions with resolutions of 3.8 Å, 4.2 Å and 4.3 Å that differed in the position of the third LF bound to PA_7 (Fig. 1A, B, Fig. S2, S3, S4) and the conformation of LF (Fig. 1C, Fig. S2, S3, S4). The densities corresponding to the lethal factors in the 4.3 Å structure were not resolved well enough to allow the fitting of an atomic model (Fig. S2F, I, S4B). Therefore, we proceeded with the remaining two structures, combined the two particle stacks and masked out the density of the third LF to improve the resolution of the rest of the complex to 3.5 Å (Fig. S2H, S3, S4D). Using a combination of the maps, we then build atomic models for the 3.8 Å and 4.2 Å reconstructions (Fig. 1A, B, Table S1).

The structures reveal that PA_7 forms a seven-fold symmetric ring structure with a ~25 Å wide central opening. With the exception of a few poorly resolved loop regions in the periphery of PA_7, our structures almost perfectly superimpose with the crystal structure of the PA_7 pre-pore (PDB:1TZO; RMSD of 0.92 Å) (26) (Fig. S5A), indicating that the binding of LF does not induce conformational changes in PA_7. This is in contrast to Ren et al. who suggested that LF binding results in a distortion of the symmetric PA_7 ring, thereby facilitating the passage of cargo through the enlarged lumen (31,37). Noteworthy, the 2β2-2β3 loop region (residues 300-323) which is implicated in pore formation was not resolved in our map. This indicates a high flexibility of this loop, which is in line with previous MD simulations (38).

In all PA_7LF_3 structures, the three LFs sit on top of PA_7. The densities corresponding to the LFs show a resolution gradient from the central N-terminal domain which is resolved best

to the peripheral C-terminal domain (Fig. S4A-D). This indicates that this region is quite flexible compared to the rest of the toxin complex. The LFs do not only interact with PA_7 but also form a continuous chain of head-to-tail interactions with each other. Binding of LF to a single PA protomer is mediated via the N-terminal domain of LF, orienting its bulky C-terminal domain such that the adjacent PA protomer is not accessible for binding. In this way a single lethal factor *de facto* occupies two of the seven binding sites of PA_7. In the chain of LFs, the C-terminal domain of the anterior LF binds to the N-terminal domain of the following one, creating a directionality in the complex (Fig. 1D). Consequently, if two LFs are bound, three free PA binding sites are available, of which only two can potentially be occupied due to steric clashes (Fig. 1D). This results in the two complexes PA_7LF_{2+1A} and PA_7LF_{2+1B}, that differ in the binding position of the third LF (Fig. 1). Since each LF occupies two potential binding sites in these structures, this leads to a symmetry mismatch and leaves one PA unoccupied.

Crucial Interactions in the PA_7LF_3 complex

LF and PA interact mainly via a large planar interface at which domain I of LF interacts with the LF/EF binding sites of two adjacent PAs (Fig. 2, Fig. S5B). The LF-PA interface is well resolved for all LFs and almost identical in the different structures (Fig. 2A, Fig. S5A, C). The interaction is primarily mediated by an extensive hydrophobic core that is further surrounded by electrostatic interactions (Fig. 2A). The interface in our structure is very similar to the one previously described for PA_8LF_4 (21). There, the second LF-PA interface is formed by the N-terminal α-helix of LF that interacts with the α-clamp located at the interface of two PAs. This "open" conformation differs from the "closed" conformation of this region as observed in the structure of the unbound LF (27). When comparing the LFs in our structure with that of the unbound LF, we observed that the C-terminal domain of the LFs in PA_7LF_3 is rotated in relation to the N-terminal domain, bringing them closer together (Fig. 3, Movie S1). However, we only found that the N-terminal region of one LF (^{2}LF) resides in the α-clamp, adopting the "open"

conformation as described for PA_8LF_4 (21). In the other LFs (^{1}LF, ^{3}LF), this region is flexible and not interacting with the α-clamp (Fig. 2B). A steric clash between the loop region (residues 576-579) of ^{1}LF and α1-β1 of ^{2}LF (Fig. 4A) prevents the N-terminal α-helix of LF from remaining in the "closed" conformation. Since these LFs neither take the "open", nor the "closed" conformation, we propose that they reside in an "intermediate" conformational state between toxin assembly and translocation. We further hypothesize that ^{2}LF is the first of the three lethal factors that is unfolded by PA_7 and is also the first one to be translocated.

As described above, the LFs interact via their N- and C-terminal regions. In two of our structures, PA_7LF_{2+1A} and PA_7LF_{2+1B}, two LFs only interact at one position which is located next to the major LF-PA interface. In the third structure, which we designate as $PA_7LF_{(2+1A)'}$, two LFs likely interact with each other also via their C-terminal region close to the central axis of the complex (Fig. 5, Movie S2). However, the position of the interaction differs from the additional interface, that has been proposed by Fabre et al. (34). At the main ^{2}LF-^{1}LF interface, the helix-loop region (residues 572-579) of the first lethal factor (^{1}LF) forms a relatively small interface with the helix-helix-β-sheet motif (residues 52-84) of the adjacent lethal factor (^{2}LF) (Fig. 4B). Residues L63, L71 and I81 of ^{2}LF form a central hydrophobic cavity that interacts with Y579 of ^{1}LF. In the β-sheet region of ^{2}LF, we identified a potential backbone-backbone hydrogen bond between K578 and I81 of ^{1}LF. In addition, P577 forms a hydrophobic interaction with Y82, which is further stabilized by H91. K572, being located on the α-helix next to the loop region in ^{1}LF, could potentially form a salt bridge interaction with E52 or D85 of ^{2}LF. Together these interactions mediate the binding between two LFs. Although the local resolution at the ^{2}LF-^{3A}LF and ^{3B}LF-^{1}LF interfaces does not allow the fitting of side chains (Fig. S4A-D), we could flexibly fit in the structures of ^{1}LF and ^{2}LF at this position. Since all structures are almost identical at backbone level (RMSD of 0.84 Å and 0.96 Å) (Fig. S5F), we expect them to exhibit a similar network of interactions. Both interfaces, LF-PA and LF-LF that

189 we describe here limit the freedom of movement mainly in the N-terminal region of LF, but
190 still allows a certain level of flexibility in the rest of the protein.

191 In all structures, the LFs show a gradient in flexibility (Fig. 1A-C, S4A-D). This was
192 previously not observed at lower resolution (34). ^{1}LF is resolved best in all structures, followed
193 by ^{2}LF and ^{3}LF has the weakest density in all reconstructions. Since the N-terminal domain is
194 well resolved in all LFs, this cannot be due to a varying occupancy of the binding sites, but
195 must stem from a flexibility of the C-terminal domain. As expected, all free C-terminal
196 domains, i.e. those that are not stabilized by an adjacent LF are more flexible than those with a
197 binding partner. However, there is one exception, namely ^{2}LF. In this case, the C-terminal
198 domain is always flexible, independent of a stabilizing binding partner. Interestingly, ^{2}LF is
199 also the only lethal factor where the N-terminal α-helix of LF is ordered and resides in the α-
200 clamp, suggesting that this interaction results in a destabilization of the C-terminal domain of
201 the molecule. This is in line with a recently reported structure of the PA_7LF_1 pore state where
202 the C-terminal domain of the single LF bound was not resolved while the N-terminal α-helix is
203 also bound to the α-clamp (36).
204
205
206 **Discussion**
207 We determined three structures of the fully-loaded heptameric anthrax lethal toxin complex,
208 which differ in the position and conformations of the bound LFs. Due to a symmetry mismatch,
209 three LFs occupy six binding sites of the heptameric PA_7 complex, leaving one PA site empty.
210 Compared to the "closed" state as observed in the crystal structure of LF (27), the C-terminal
211 domain of the LFs in PA_7LF_3 is rotated respective to the N-terminal domain. However, only
212 ^{2}LF adopts the "open" conformation which was reported for the structure of PA_8LF_4 (21), i.e.
213 the N-terminal α-helix interacts with the α-clamp of PA. ^{1}LF and ^{3}LF do not show this
214 interaction, but can also not be in the "closed" conformation because of a steric clash with an

adjacent LF. We therefore propose that they are in an "intermediate" state between toxin assembly and translocation.

Why has this state not been observed in the crystal structure of PA_8LF_4? It could have been missed due to averaging of the asymmetric unit of the PA_8LF_4 crystals, which is composed of two PAs and one LF. Another possibility is that compared to PA_7, the PA_8 pre-pore provides more space for the N-termini of the LFs to arrange in the "open" conformation in comparison to the PA_7 pre-pore. However, if all LFs were indeed in a "ready-to-be-translocated position" which LF would then be translocated first through the narrow PA pore that only allows the passage of a single unfolded LF at a time? The process could in principle be stochastic, but our PA_7LF_3 structures offer an alternative explanation.

Already based on the low-resolution structure of the PA_7LF_3 pre-pore (34), it has been suggested that the order of translocation is non-stochastic and that the first LF, whose N-terminal domain is not interacting with an adjacent LF, is translocated first. After the translocation of this factor, the second LF would be released from the inhibitory bond of the first LF and then be translocated and so on (34). However, our data indicate that this chain reaction is rather unlikely.

Although we can as well only speculate about the exact order of translocation, based on our cryo-EM structures, two alternative scenarios are conceivable: In the first one, the factor in the "open" state, ^{2}LF, is translocated first, followed by ^{1}LF or ^{3}LF which are in the "intermediate" state. The second possibility would be that ^{1}LF and ^{3}LF are translocated before ^{2}LF. Due to the different arrangements in the complexes, both alternatives exclude a chain reaction. In addition, the translocation is not triggered or blocked by an adjacent LF.

While we cannot exclude the second scenario, we think that the first one is more likely. Being in the "open" conformation, the N-terminal α-helix of ^{2}LF interacts with the α-clamp of PA. Similar to other unfolding machineries such as ClpA/Hsp100 (39), the α-clamp is known to unfold polypeptides in a sequence-independent manner. The current theory is that it first

stabilizes unfolding intermediates, and introduces mechanical strain before the unfolded structure is fed further down the central pore (21). In this way it would facilitate the rapid unfolding of the entire ^{2}LF molecule upon transition into the pore state. We therefore believe that ^{2}LF is translocated before ^{1}LF and ^{3}LF. The higher flexibility in the C-terminal domain of ^{2}LF in the presence of potentially stabilizing neighboring LFs suggests that the interaction of the N-terminal domain with the α-clamp results in a destabilization of the molecule. This in turn lowers the energy barrier for the unfolding of the entire LF molecule and further supports the assumption that ^{2}LF is translocated first. Once ^{2}LF is translocated, either ^{1}LF or ^{3}LF can follow. As these two LFs both adopt an "intermediate" conformation in our structures, we cannot predict which LF is translocated next.

We propose that ^{2}LF is not only the first LF being translocated, but also the first one that binds to PA_7 during toxin assembly and predict the following model (Fig. 6). Upon binding to PA, ^{2}LF undergoes a conformational change from the "closed" to the "open" state (Fig. 6A, B). In the next step, ^{1}LF binds to the position next to ^{2}LF (Fig. 6C). Instead of transitioning into the "open" conformation, it adopts an "intermediate" conformation. The third LF binds in a similar manner, but can attach to two different PA sites, resulting in two different complexes (Fig. 6D). In this way, the assembled toxin has three LFs bound to PA_7 with two in an "intermediate" and one in the "open" conformation (Fig. 6D).

In summary, our high-resolution cryo-EM structures provide us with novel insights into the organization of the fully-loaded heptameric anthrax lethal toxin and thus advance our understanding of toxin assembly and translocation.

Material and Methods

Protein expression and purification

Protective antigen (PA) from *Bacillus anthracis* was cloned into a pET19b vector (Novagen), resulting in a N-terminal His_{10}-tag fusion construct. *E. coli* BL21(DE3) were transformed with the pET19b::His_{10}-PA plasmid and expression was induced immediately after transformation by the addition of 75 µM IPTG. Following incubation at 28 °C for 24 h in LB medium, cells were pelleted, resuspended in lysis-buffer (20 mM Tris-HCl pH 8.5, 300 mM NaCl, 500 µM EDTA, 5 µg/ml DNAse, 1 mg/ml Lysozym plus Protease inhibitor cOmplete tablets from Sigma Aldrich) and lysed by sonication. Soluble proteins were separated from cell fragments by ultracentrifugation (15,000 rpm, 45 min, 4°C) and loaded onto Ni-IDA beads (Cube Biotech). After several washing steps, the protein was eluted with elution buffer (500 mM imidazole, 20 mM Tris-HCl pH 8.5, 500 mM NaCl, 1 mM EDTA). Protein-containing fractions were pooled and dialyzed against buffer containing 50 mM Tris-HCl pH 8.5, 150 mM NaCl, 1 mM EDTA. Subsequently, the sample was further purified using anion-exchange Mono Q (GE Healthcare) with a no-salt buffer (20 mM Tris-HCl pH 8.5) and high-salt buffer (20 mM Tris-HCl pH 8.5, 1M NaCl), applying a gradient from 0 to 40%. Next, oligomerization of PA was induced by addition of trypsin (1 µg enzyme for each mg of PA), followed by incubation on ice for 30 min. Upon addition of double molar excess of trypsin inhibitor (Sigma Aldrich), PA_7 was further purified by size exclusion chromatography using a Superdex 200 column (GE Healthcare). Lyophilized LF (List Biological Lab. Inc., Lot#1692A1B) were resuspended in water according to the manufacturer's manual and mixed with PA_7 in a molar ration of 10:1. Ultimately, loaded complexes were further purified in a final size exclusion chromatography step (20 mM Tris-HCl pH 8.5, 150 mM NaCl) using a Superdex 200i column (GE Healthcare), before being used in down-stream applications.

Reconstitution of PA_7 in lipid-mimetic systems

For nanodisc insertion, Ni-NTA column material was first washed with ddH_20 and subsequently equilibrated with buffer A (50 mM NaCl, 20 mM Tris-HCl – pH 8.5, 0.05 % Octyl β-D-glucopyranoside (w/v)). In the next step, 500 µL of 0.2 µM PA_7 in the pre-pore state was added and incubated for 25 min at room temperature. An additional washing step with buffer A was performed to remove unbound PA_7 pre-pore, followed by a 5 min incubation step with 1 M urea at 37°C and another wash with buffer A. MSP1D1:POPC:sodium cholate ratio and preparation was done according to Akkaladevi et al (33). After dialysis (MWCO of 12-14k) for 24 to 72 h against buffer B (50 mM NaCl, 20 mM Tris-HCl pH 7.5), excess of nanodiscs was collected from five washing steps with 500 µL of buffer B. To elute PA_7 pores inserted into nanodiscs, column material was incubated for 10 min on ice in buffer C (500 mM NaCl, 50 mM Tris-HCl pH 7.5, 50 mM imidazole). The eluted sample was concentrated and subsequently used for negative staining EM.

For the preparation of pre-formed liposomes, POPC was initially solubilized in 5 % OG. Solubilized lipids were dialyzed (MWCO: 12-14k) for 8 - 12 h at 4°C against buffer A and subsequently PA_7 pre-pores were added to the lipids in a 1 : 10 molar ratio. Following 24 – 72 h dialysis (MWCO:12-14k) against buffer D (50 mM NaCl 50 mM NaOAc, pH 5.0), samples were used for negative staining EM.

Negative-stain electron microscopy

Complex purity and integrity were assessed by negative stain electron microscopy prior to cryo-EM grid preparation and image acquisition. For negative stain, 4 µl of purified PA_7LF_3 complex at a concentration of ~0.04 mg/ml was applied onto a freshly glow discharged carbon-coated copper grid (Agar Scientific; G400C) and incubated for 45 s. Subsequently, excess liquid was blotted away with Whatman no. 4 filter papers. The sample was stained with 0.8 % (w/v) uranyl acetate (Sigma Aldrich). Micrographs were recorded manually using a JEOL JEM-1400 TEM,

operated at an acceleration voltage of 120 kV, equipped with a 4,000 × 4,000 CMOS detector F416 (TVIPS) and a pixel size of 1.84 Å/px.

Sample vitrification

For Cryo-EM sample preparation, 4 µl of purified PA_7LF_3 at a concentration of ~0.06 mg/ml was applied onto freshly glow discharged grids (Quantifoil R 1.2/1.3 holey carbon with a 2 nm additional carbon support) and incubated for 45 s. Subsequently, grids were blotted automatically and plunged into liquid ethane using a CryoPlunge3 (Gatan) at a humidity of ~ 95 %. Grid quality was screened before data collection using a JEOL JEM-1400 TEM electron microscope (same settings as for negative-stain electron microscopy) or with an Arctica microscope (FEI), operated at 200 kV. Grids were kept in liquid nitrogen for long-term storage.

Cryo-EM data acquisition

Cryo-EM data sets of PA_7LF_3 were collected on a Titan Krios transmission electron microscope (FEI) equipped with a high-brightened field-emission gun (XFEG), operated at an acceleration voltage of 300 kV. Micrographs were recorded on a K2 direct electron detector (Gatan) at 130,000 x magnification in counting mode, corresponding to a pixel size of 1.07 Å. 40 frames taken at intervals of 375 ms (1.86 $e^-/Å^2$) were collected during each exposure, resulting in a total exposure time of 15 s and total electron dose of 74.4 $e^-/Å^2$. Using the automated data collection software EPU (FEI), a total of 5238 micrographs with a defocus range between -1.2 and -2.6 µm was automatically collected.

Image processing and 3-D reconstruction

Micrographs of the dataset were inspected visually and ones with extensive ice contamination or high drift were discarded. Next, frames were aligned and summed using MotionCor2 (in 3 x 3 patch mode) (40). By doing so, dose-weighted and un-weighted full-dose images were

generated. Image and data processing were performed with the SPHIRE/EMAN2 software package (41). Un-weighted full-dose images were used for defocus and astigmatism estimation by CTER. With the help of the drift assessment tool in SPHIRE, drift-corrected micrographs were further sorted to discard high defocus as well as high drift images that could not be compensated for by frame alignment.

For the PA_7LF_3 dataset, particles were automatically selected based on a trained model using the crYOLO software, implemented in SPHIRE (42). In total, 382 k particles were extracted from the dose-weighted full dose images with a final window size of 336 x 336 pixel. Two-dimensional classification was performed using the iterative and stable alignment and clustering (ISAC) algorithm implemented in SPHIRE. Several rounds of 2-D classification yielded a total number of 213 k 'clean' dose-weighted and drift-corrected particles. During the manual inspection of the 2-D class averages, top views of the particles were excluded.

A generated composite crystal structure consisting of PA_7 (PDB:1TZO) decorated with three full-length LF (PDB:1J7N), docked with their N-terminal domain to PA as observed in the PA_8LF_4 structure (PDB: 3KWV), was converted into electron density (sp_pdb2em functionality in SPHIRE). After filtering to 30 Å, this map served as reference in the subsequent 3-D refinement. The 3-D refinement without imposed symmetry (sxmeridien in SPHIRE, C1) yielded an initial 3.5 Å electron density map of the PA_7LF_3 complex. Several rounds of 3-D classification and rotation of certain classes were necessary to separate particles belonging to PA_7LF_{2+1A}, PA_7LF_{2+1B} and $PA_7LF_{(2+1A)'}$ complexes. The flowchart of the image processing strategy including the obtained 3-D classes as well as the number of particles that they contained is described in detail in Fig. S3.

Global resolutions of the final maps were calculated between two independently refined half maps at the 0.143 FSC criterion, local resolution was calculated using sp_locres in SPHIRE. The final densities were filtered according to local resolution or the local de-noising filter

LAFTER was applied to recover features with more signal than noise (based on half maps) (43).

Model building, refinement and validation

To build the PA_7 model, a single monomer of the PA_7 crystal structure (PDB:1TZO) was used as starting model and a preliminary fit into the PA density of the $PA_7LF_{3\text{-masked}}$ map was done using rigid body fitting in Chimera. Next, it was flexibly fitted into the corresponding density using iMODFIT (44). The resulting model was copied and fitted to the other six PA densities and each monomer was separately refined further using a combination of manual model building in COOT and real-space refinement in PHENIX. Subsequently, all seven monomers were merged together to create the final model of PA_7. Unresolved loop regions were deleted (275-285, 301-322, 424-428 and 644-656) and less resolved regions exchanged to poly-A (641, 666-700, 710-715 and 720-735).

For the model building of the lethal factors, a composite model of residues 29 to 250 from the N-terminal domain of LF (PDB:3KWV) and residues 251 to 773 from the full-length LF structure (PDB:1J7N) was generated. This hybrid pdb served as staring model and was initially fitted into the density of ^{1}LF and ^{2}LF in the $PA_7LF_{3\text{-masked}}$ structure using rigid body fitting in Chimera. In the next step, models were flexibly fitted into the density using iMODFIT, followed by further refinement using a combination of manual model building in COOT and real-space refinement in PHENIX for ^{1}LF (52-254 and 550-600) and ^{2}LF (32-253).

The resulting models for ^{1}LF, ^{2}LF and PA_7 served again as starting point for the PA_7LF_{2+1B} structure and were flexibly fitted into the corresponding density. Additional refinement using a combination of manual model building in COOT and real-space refinement in PHENIX was performed for ^{1}LF (52-254 and 550-600) and ^{2}LF (32-253), similar as in the $PA_7LF_{3\text{-masked}}$ structure. The density for the N-terminal domain of ^{3}LF was less well resolved and therefore

393 only flexibly fitted into the density using iMODFIT (52-254), whereas the C-terminal domain
394 was fitted using the 'rigid body fit' tool in Chimera.
395 Like for the PA_7LF_{2+1B} structure, obtained models of ^{1}LF, ^{2}LF, ^{3}LF (of the PA_7LF_{2+1B} structure)
396 and PA_7, were flexibility fitted into the PA_7LF_{2+1A} density map to obtain the final model of
397 PA_7LF_{2+1A}. The C-terminal domain of ^{3}LF was fitted using the 'rigid body fit' tool in Chimera.
398 Geometries of the final refined models were obtained from PHENIX with data statistics
399 summarized in Table S1.
400

401 **Structure analysis and visualization**

402 UCSF Chimera was used for structure analysis, visualization and figure preparation. The
403 angular distribution plots as well as beautified 2-D class averages were calculated using
404 SPHIRE.
405

406 **Acknowledgments**

407 We thank O. Hofnagel and D. Prumbaum for assistance with data collection. This work was
408 supported by the Max Planck Society (to S.R.) and the European Council under the European
409 Union's Seventh Framework Programme (FP7/ 2007–2013) (grant no. 615984) (to S.R.). D.Q.
410 is a fellow of Fonds der Chemischen Industrie.
411

412 **Author contributions**

413 S.R. designed the project. K.A. and A.E.L. provided protein complexes. C.A. prepared
414 specimens, recorded and processed the EM data. C.A., D.Q. and C.G. analyzed the data. D.Q.
415 prepared figures. S.R. managed the project. D.Q. and S.R. wrote the manuscript with input from
416 all authors.
417
418

Competing interests

The authors declare no competing financial interests.

Data availability

The cryo-EM density maps of the PA_7LF_{2+1A}, PA_7LF_{2+1B} and $PA_7LF_{(2+1A)'}$, complexes are deposited into the Electron Microscopy Data Bank with the accession codes EMD-xxxx, EMD-xxxx and EMD-xxxx, respectively. Corresponding coordinates for PA_7LF_{2+1A} and PA_7LF_{2+1B} have been deposited in the Protein Data Bank under accession number xxxx and xxxx. Relevant data and details of plasmids and strains are available from the corresponding author upon reasonable request.

References

1. World Health Organization. Anthrax in humans and animals. 2008.

2. O'Brien J, Friedlander A, Dreier T, Ezzell J, Leppla S. Effects of anthrax toxin components on human neutrophils. Infection and immunity. American Society for Microbiology Journals; 1985 Jan;47(1):306–10.

3. Friedlander AM. Macrophages are sensitive to anthrax lethal toxin through an acid-dependent process. J Biol Chem. American Society for Biochemistry and Molecular Biology; 1986 Jun 5;261(16):7123–6.

4. Sandvig K, van Deurs B. Membrane traffic exploited by protein toxins. Annual review of cell and developmental biology. 2002;18(1):1–24.

5. Friebe S, van der Goot FG, Bürgi J. The Ins and Outs of Anthrax Toxin. Toxins. 2016 Mar;8(3):69.

6. Leppla SH. Anthrax toxin edema factor: a bacterial adenylate cyclase that increases cyclic AMP concentrations of eukaryotic cells. Proceedings of the National Academy of Sciences. National Academy of Sciences; 1982 May 1;79(10):3162–6.

7. Duesbery NS, Webb CP, Leppla SH, Gordon VM, Klimpel KR, Copeland TD, et al. Proteolytic Inactivation of MAP-Kinase-Kinase by Anthrax Lethal Factor. Science. American Association for the Advancement of Science; 1998 May 1;280(5364):734–7.

8. Bradley KA, Mogridge J, Mourez M, Collier RJ, Young JAT. Identification of the cellular receptor for anthrax toxin. Nature. Nature Publishing Group; 2001 Nov 1;414(6860):225–9.

452 9. Scobie HM, Rainey GJA, Bradley KA, Young JAT. Human capillary morphogenesis
453 protein 2 functions as an anthrax toxin receptor. Proceedings of the National Academy
454 of Sciences. National Academy of Sciences; 2003 Apr 29;100(9):5170–4.

455 10. Klimpel KR, Molloy SS, Thomas G, Leppla SH. Anthrax toxin protective antigen is
456 activated by a cell surface protease with the sequence specificity and catalytic
457 properties of furin. Proceedings of the National Academy of Sciences. National
458 Academy of Sciences; 1992 Nov 1;89(21):10277–81.

459 11. Milne JC, Furlong D, Hanna PC, Wall JS, Collier RJ. Anthrax protective antigen forms
460 oligomers during intoxication of mammalian cells. J Biol Chem. American Society for
461 Biochemistry and Molecular Biology; 1994 Aug 12;269(32):20607–12.

462 12. Kintzer AF, Thoren KL, Sterling HJ, Dong KC, Feld GK, Tang II, et al. The protective
463 antigen component of anthrax toxin forms functional octameric complexes. Journal of
464 molecular biology. 2009 Sep 25;392(3):614–29.

465 13. Abrami L, Liu S, Cosson P, Leppla SH, van der Goot FG. Anthrax toxin triggers
466 endocytosis of its receptor via a lipid raft–mediated clathrin-dependent process. The
467 Journal of Cell Biology. 2003 Jan 27;160(3):321–8.

468 14. Kintzer AF, Sterling HJ, Tang II, Abdul-Gader A, Miles AJ, Wallace BA, et al. Role of
469 the Protective Antigen Octamer in the Molecular Mechanism of Anthrax Lethal Toxin
470 Stabilization in Plasma. Journal of molecular biology. 2010;399(5):741–58.

471 15. Pimental R-AL, Christensen KA, Krantz BA, Collier RJ. Anthrax toxin complexes:
472 heptameric protective antigen can bind lethal factor and edema factor simultaneously.
473 Biochemical and biophysical research communications. Academic Press; 2004 Sep
474 10;322(1):258–62.

16. Abrami L, Bischofberger M, Kunz B, Groux R, van der Goot FG. Endocytosis of the Anthrax Toxin Is Mediated by Clathrin, Actin and Unconventional Adaptors. T Young JA, editor. PLoS Pathogens. Public Library of Science; 2010 Mar 1;6(3):e1000792.

17. Boll W. Effects of dynamin inactivation on pathways of anthrax toxin uptake. European Journal of Cell Biology. Urban & Fischer; 2004 Jan 1;83(6):281–8.

18. Carl J Miller, Jennifer L Elliott A, Collier RJ. Anthrax Protective Antigen: Prepore-to-Pore Conversion†. Vol. 38, Biochemistry. American Chemical Society; 1999. 10 p.

19. Jiang J, Pentelute BL, Collier RJ, Zhou ZH. Atomic structure of anthrax protective antigen pore elucidates toxin translocation. Nature. Nature Publishing Group; 2015 May 28;521(7553):545–9.

20. Krantz BA, Melnyk RA, Zhang Sen, Juris SJ, Lacy DB, Wu Z, et al. A Phenylalanine Clamp Catalyzes Protein Translocation Through the Anthrax Toxin Pore. Science. American Association for the Advancement of Science; 2005 Jul 29;309(5735):777–81.

21. Feld GK, Thoren KL, Kintzer AF, Sterling HJ, Tang II, Greenberg SG, et al. Structural basis for the unfolding of anthrax lethal factor by protective antigen oligomers. Nature structural & molecular biology. Nature Publishing Group; 2010 Nov;17(11):1383–90.

22. Krantz BA, Trivedi AD, Cunningham K, Christensen KA, Collier RJ. Acid-induced unfolding of the amino-terminal domains of the lethal and edema factors of anthrax toxin. Journal of molecular biology. 2004 Nov 26;344(3):739–56.

23. Wynia-Smith SL, Brown MJ, Chirichella G, Kemalyan G, Krantz BA. Electrostatic ratchet in the protective antigen channel promotes anthrax toxin translocation. The

Journal of biological chemistry. American Society for Biochemistry and Molecular Biology; 2012 Dec 21;287(52):43753–64.

24. Tamayo AG, Slater L, Parker JT, Bharti A, Harrison R, Hung DT, et al. GRP78(BiP) facilitates the cytosolic delivery of anthrax lethal factor (LF) in vivo and functions as an unfoldase in vitro. Molecular Microbiology. John Wiley & Sons, Ltd; 2011 Sep 1;81(5):1390–401.

25. Slater LH, Hett EC, Clatworthy AE, Mark KG, Hung DT. CCT chaperonin complex is required for efficient delivery of anthrax toxin into the cytosol of host cells. Proceedings of the National Academy of Sciences. National Academy of Sciences; 2013 Jun 11;110(24):9932–7.

26. Petosa C, Collier RJ, Klimpel KR, Leppla SH, Liddington RC. Crystal structure of the anthrax toxin protective antigen. Nature. Nature Publishing Group; 1997 Feb 1;385(6619):833–8.

27. Pannifer AD, Wong TY, Schwarzenbacher R, Renatus M, Petosa C, Bienkowska J, et al. Crystal structure of the anthrax lethal factor. Nature. Nature Publishing Group; 2001 Nov 1;414(6860):229–33.

28. Drum CL, Yan S-Z, Bard J, Shen Y-Q, Lu D, Soelaiman S, et al. Structural basis for the activation of anthrax adenylyl cyclase exotoxin by calmodulin. Nature. Nature Publishing Group; 2002 Jan 1;415(6870):396–402.

29. Shen Y, Zhukovskaya NL, Guo Q, Florián J, Tang W-J. Calcium-independent calmodulin binding and two-metal–ion catalytic mechanism of anthrax edema factor. The EMBO Journal. John Wiley & Sons, Ltd; 2005 Mar 9;24(5):929–41.

519 30. Santelli E, Bankston LA, Leppla SH, Liddington RC. Crystal structure of a complex
520 between anthrax toxin and its host cell receptor. Nature. 2004 Aug;430(7002):905–8.

521 31. Ren G, Quispe J, Leppla SH, Mitra AK. Large-Scale Structural Changes Accompany
522 Binding of Lethal Factor to Anthrax Protective Antigen: A Cryo-Electron Microscopic
523 Study. Structure. Cell Press; 2004 Nov 1;12(11):2059–66.

524 32. Tama F, Ren G, Brooks CL, Mitra AK. Model of the toxic complex of anthrax:
525 responsive conformational changes in both the lethal factor and the protective antigen
526 heptamer. Protein science : a publication of the Protein Society. 2006 Sep;15(9):2190–
527 200.

528 33. Akkaladevi N, Hinton-Chollet L, Katayama H, Mitchell J, Szerszen L, Mukherjee S, et
529 al. Assembly of anthrax toxin pore: lethal-factor complexes into lipid nanodiscs.
530 Protein science : a publication of the Protein Society. 2013 Apr;22(4):492–501.

531 34. Fabre L, Santelli E, Mountassif D, Donoghue A, Biswas A, Blunck R, et al. Structure
532 of anthrax lethal toxin prepore complex suggests a pathway for efficient cell entry. The
533 Journal of general physiology. 2016 Oct;148(4):313–24.

534 35. Gogol EP, Akkaladevi N, Szerszen L, Mukherjee S, Chollet-Hinton L, Katayama H, et
535 al. Three dimensional structure of the anthrax toxin translocon-lethal factor complex by
536 cryo-electron microscopy. Protein science : a publication of the Protein Society. 2013
537 May;22(5):586–94.

538 36. Hardenbrook NJ, Liu S, Zhou K, Ghosal K, Zhou ZH, Krantz BA. Atomic structures of
539 anthrax toxin protective antigen channels bound to partially unfolded lethal and edema
540 factors. Nature Communications. Nature Publishing Group; 2020 Feb 11;11(1):1–10.

541 37. Lacy DB, Wigelsworth DJ, Melnyk RA, Harrison SC, Collier RJ. Structure of
542 heptameric protective antigen bound to an anthrax toxin receptor: A role for receptor in
543 pH-dependent pore formation. Proceedings of the National Academy of Sciences. 2004
544 Sep;101(36):13147–51.

545 38. Alisaraie L, Rouiller I. Molecular assembly of lethal factor enzyme and pre-pore
546 heptameric protective antigen in early stage of translocation. J Mol Model. Springer
547 Berlin Heidelberg; 2016 Jan 1;22(1):1–12.

548 39. Hinnerwisch J, Fenton WA, Furtak KJ, Farr GW, Horwich AL. Loops in the Central
549 Channel of ClpA Chaperone Mediate Protein Binding, Unfolding, and Translocation.
550 Cell. Cell Press; 2005 Jul 1;121(7):1029–41.

551 40. Zheng SQ, Palovcak E, Armache J-P, Verba KA, Cheng Y, Agard DA. MotionCor2:
552 anisotropic correction of beam-induced motion for improved cryo-electron microscopy.
553 Nature methods. Nature Publishing Group; 2017 Apr;14(4):331–2.

554 41. Moriya T, Saur M, Stabrin M, Merino F, Voicu H, Huang Z, et al. High-resolution
555 Single Particle Analysis from Electron Cryo-microscopy Images Using SPHIRE.
556 Journal of visualized experiments : JoVE. 2017 May 16;(123).

557 42. Wagner T, Merino F, Stabrin M, Moriya T, Antoni C, Apelbaum A, et al. SPHIRE-
558 crYOLO is a fast and accurate fully automated particle picker for cryo-EM. Commun
559 Biol. Nature Publishing Group; 2019 Jun 19;2(1):218–13.

560 43. Ramlaul K, Palmer CM, Aylett CHS. A Local Agreement Filtering Algorithm for
561 Transmission EM Reconstructions. Journal of Structural Biology. Academic Press;
562 2019 Jan 1;205(1):30–40.

563 44. Lopéz-Blanco JR, Chacón P. iMODFIT: Efficient and robust flexible fitting based on
564 vibrational analysis in internal coordinates. Journal of Structural Biology. Academic
565 Press; 2013 Nov 1;184(2):261–70.

566

Figure captions

Figure 1. Cryo-EM structures of the PA_7LF_3 complexes.

(**A**) Top view and side view of the color-coded segmented cryo-EM density map of PA_7LF_{2+1A}, with PA_7 in blue, ^{1}LF in pink, ^{2}LF in gold and ^{3}LF in cyan. Three lethal factors bind to the PA_7 ring and form a continuous chain of head-to-tail interactions. Schematic representation is shown on the left, corresponding atomic model on the right. (**B**) Same as in (A) for the PA_7LF_{2+1B} complex. (**C**) Same as in (A) for the $PA_7LF_{(2+1A)'}$ complex. Notably, two LFs interact in their peripheral region (C-terminal domain) with each other close to the central axis. Segmented maps are shown at different thresholds for visualization. (**D**) Schematic representation of the last step in PA_7LF_3 toxin assembly, in which the third lethal factor can bind to one of two empty PA sites, resulting in two different complexes, PA_7LF_{2+1A} and PA_7LF_{2+1B}. Top and side views are shown, with the same color code as in (A), except that PA protomers alternate in light and dark blue.

Figure 2. Interfaces between lethal factor and protective antigen.

(**A**) The N-terminal domain of LF mediates binding to two adjacent PA molecules, forming a large planar interface. The positions of ^{2}LF (gold), PA and PA'(blue) are shown relative to the overall shape of the complex that is represented as transparent, low-pass filtered volume. A black square indicates the interaction interface between all three molecules. The inset shows a close-up of the interaction regions, with contributing residues labeled. They form a central hydrophobic core, that is surrounded by electrostatic interactions. (**B**) The second LF-PA interface is formed by the N-terminal α-helix of LF, interacting with the α-clamp region, located between two adjacent PA molecules. The four panels depict a close-up of this region for the three different LFs (^{3}LF can adopt two different positions, i.e. the PA_7LF_{2+1A} or

592 PA_7LF_{2+1B} complex) with half-transparent densities shown for PA (white), PA' (light blue) and
593 the LF (^{1}LF - pink; ^{2}LF - gold; ^{3}LF – cyan). Notably, only ^{2}LF interacts with the α-clamp.
594
595 **Figure 3. Conformational change of LF upon PA binding.**

596 Superposition of ^{1}LF (green), ^{2}LF (yellow) and unbound LF (green, PDB: 1J7N), aligned via
597 their N-terminal domains. Red and green arrows indicate similar positions in ^{1}LF and unbound
598 LF, respectively. When compared with the crystal structure of the unbound lethal factor, the
599 three LFs undergo a conformational change upon interaction with PA_7. The C-terminal domain
600 rotates with respect to the N-terminal domain such that the LFs come closer to form a
601 continuous chain of head-to-tail interactions. A schematic representation illustrates the rotation
602 of the C-terminal domain that occurs between unbound (green) and bound (red) LF
603 conformation. See also movie S1.
604
605 **Figure 4. Molecular interface between two lethal factors.**

606 (**A**) Potential steric clash between the C-terminal domain of LF (red) and the N-terminal domain
607 of an adjacent LF when it adopts the "closed" conformation (blue). The clash is highlighted as
608 fading red spot in the background. In contrast, the "open" conformation (gold), i.e. the N-
609 terminal α-helix interacts with the α-clamp region of PA, does not result in a steric clash. (**B**)
610 A relatively small interaction interface mediates binding of the C-terminal domain of LF to the
611 N-terminal domain of an adjacent LF. The positions of ^{1}LF (pink) and ^{2}LF (gold) are shown
612 relative to the overall shape of the complex that is represented as transparent, low-pass filtered
613 volume. A black square indicates the interaction interface between the two LFs. Insets show
614 close-ups of the interacting regions in different orientations, with contributing residues labeled.
615
616

617 **Figure 5. LFs can interact via their C-terminal domain.**

618 Top and side views of the low-passed filtered maps of the three PA_7LF_3 complexes, with
619 PA_7LF_{2+1B} in orange, PA_7LF_{2+1A} in yellow and $PA_7LF_{(2+1A)'}$ in light blue. Volumes are shown
620 at the same threshold. While the three LFs interact in all structures via their N- and C-terminal
621 domains in a head-to-tail manner, an additional interface was identified in the $PA_7LF_{(2+1A)'}$
622 reconstruction. Here, the C-terminal domains of ^{1}LF and ^{2}LF, interact with each other close to
623 the central axis of the PA_7LF_3 complex. This region is highlighted by dashed red circles. See
624 also movie S2.

625

626 **Figure 6. Model for PA_7LF_3 assembly.**

627 (**A**) After PA_7 formation on the surface of the host cell, (**B**) ^{2}LF binds to PA_7 and its N-terminal
628 α-helix interacts with the α-clamp region of PA, characteristic for the "open" conformation.
629 (**C**) In the next step, ^{1}LF binds adjacent to ^{2}LF. Instead of undergoing a conformational change
630 from "closed" to "open" state, it adopts an "intermediate" state. (**D**) Binding of the third LF is
631 similar as for ^{1}LF, resulting in a continuous chain of head-to-tail interactions. However, it can
632 attach to two different PA sites, resulting in two different PA_7LF_3 complexes. In this way, one
633 LF adopts the "open" conformation, whereas the other two LFs remain in an "intermediate"
634 state.

635

636 **Figures**

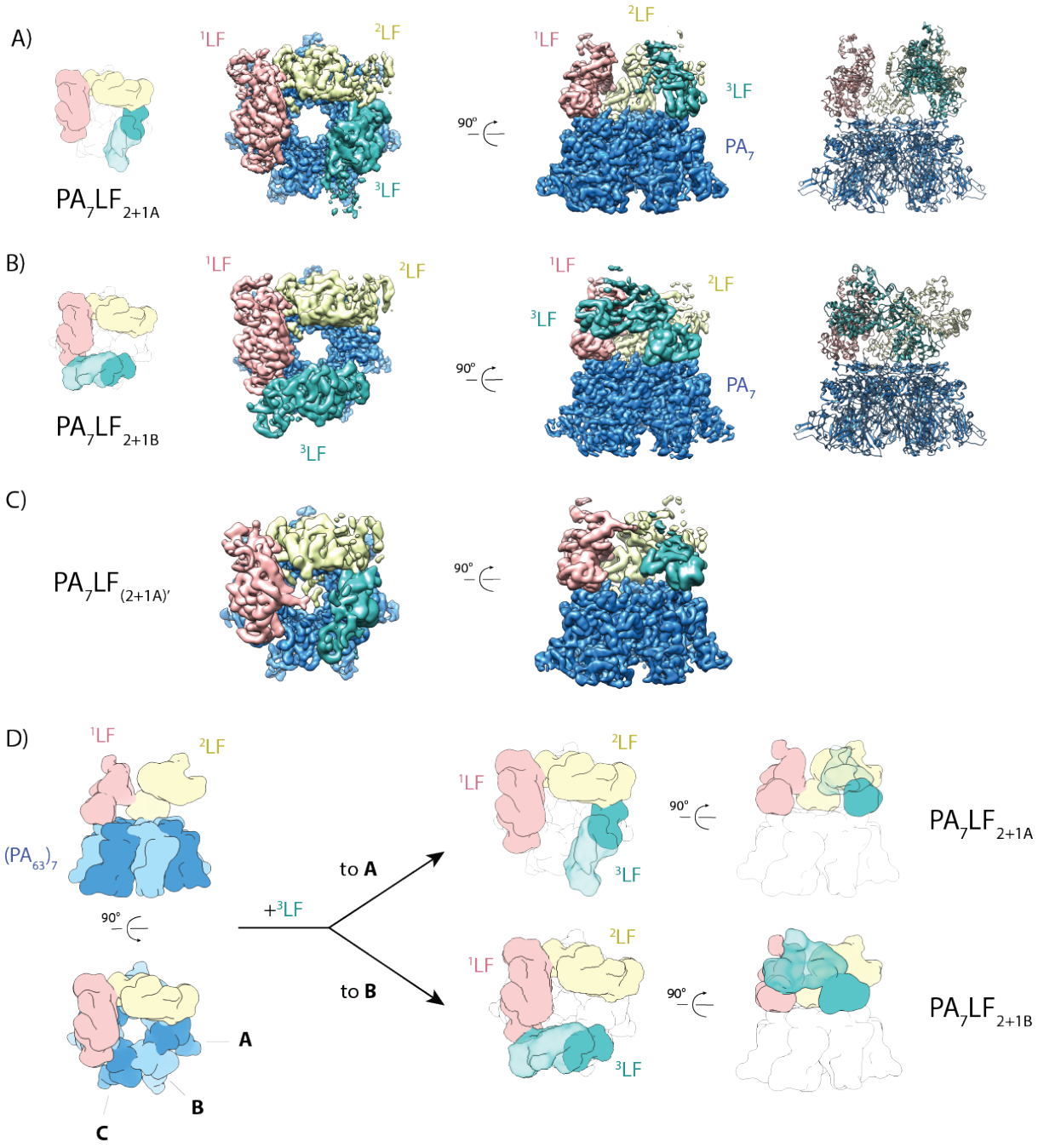

637

638 **Figure 1. Cryo-EM structures of the PA_7LF_3 complexes.**

639

640

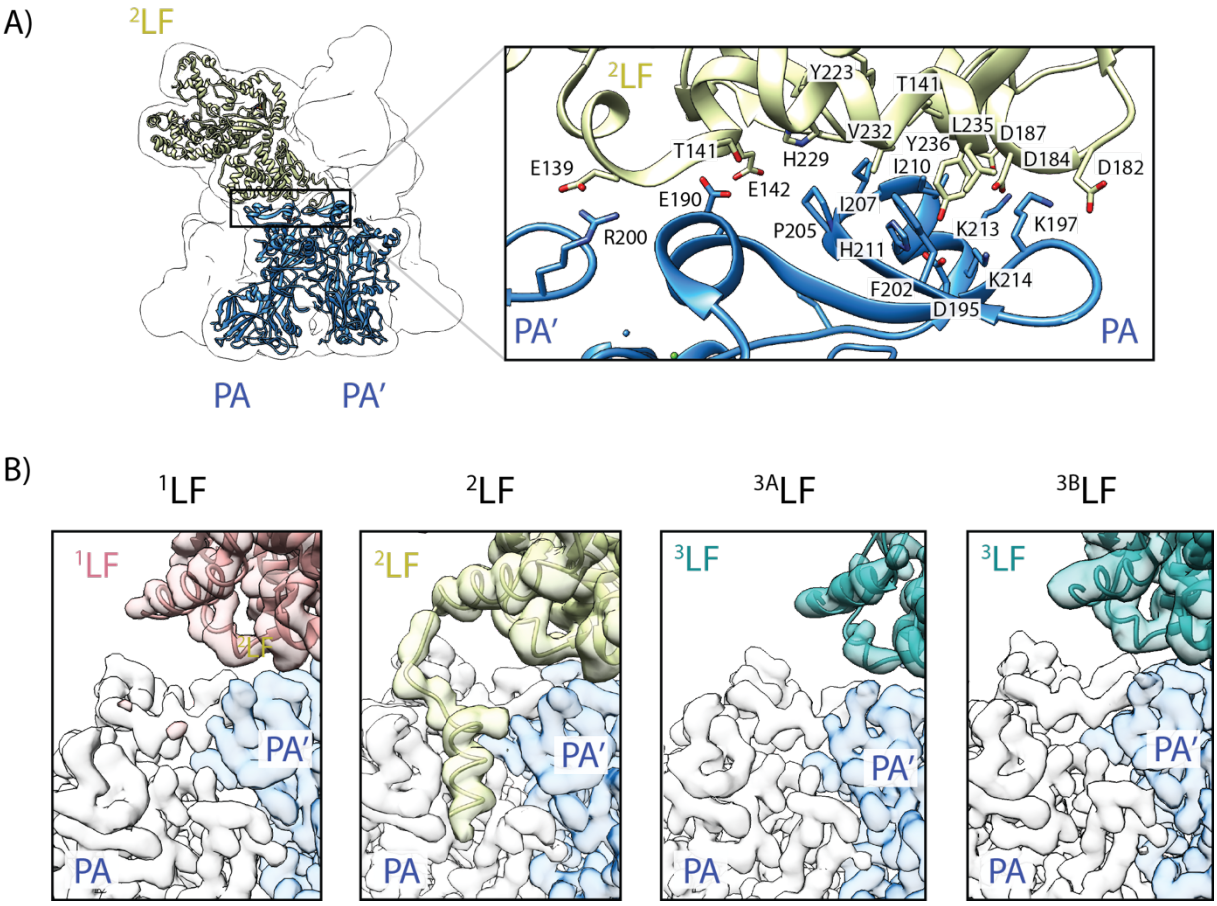

Figure 2. Interfaces between lethal factor and protective antigen.

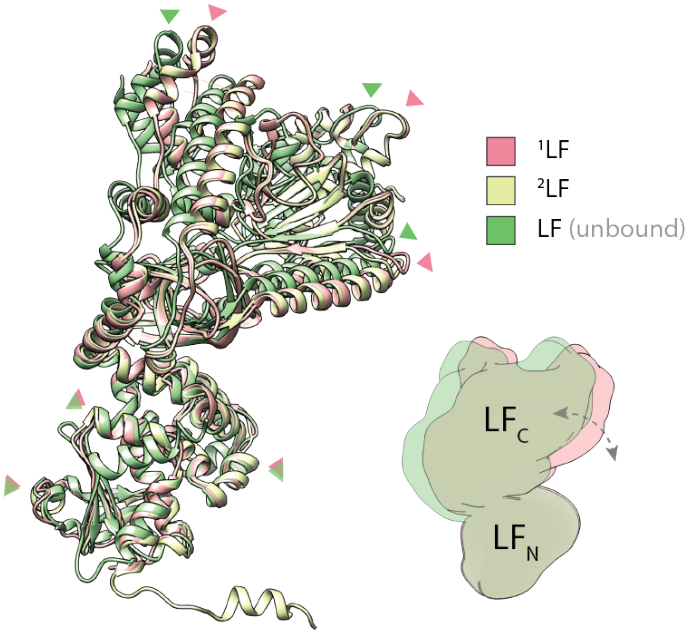

643

644 **Figure 3. Conformational change of LF upon PA binding.**

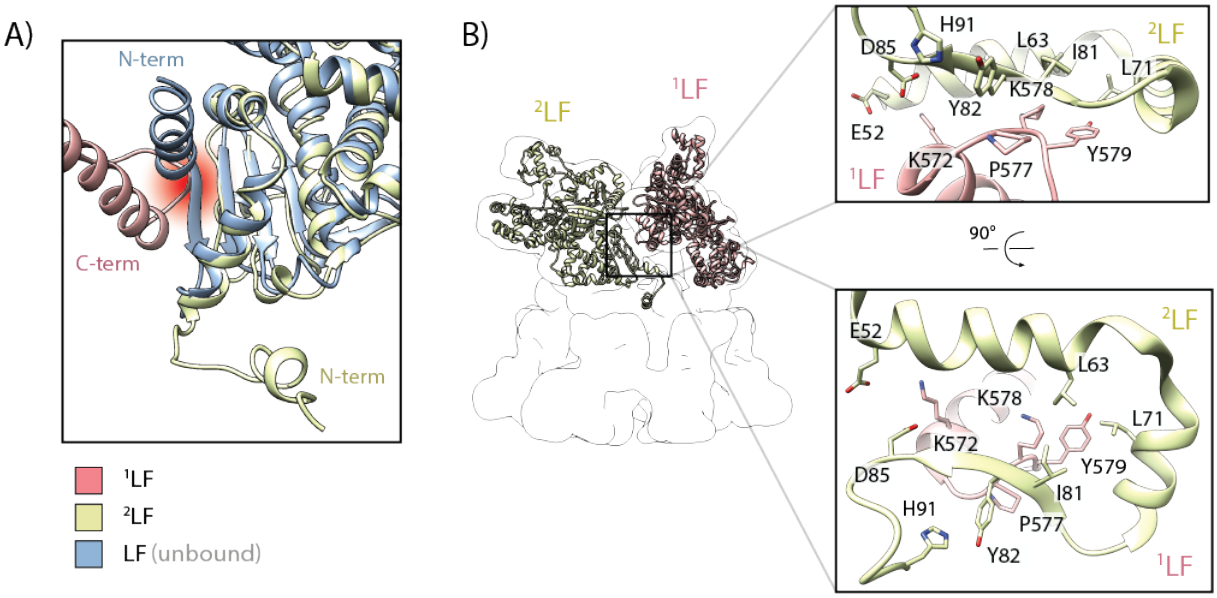

Figure 4. Molecular interface between two lethal factors.

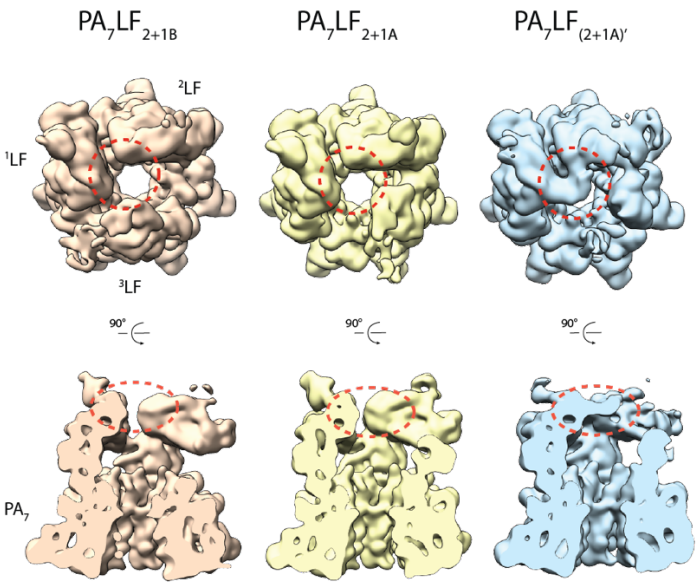

Figure 5. LFs can interact via their C-terminal domain.

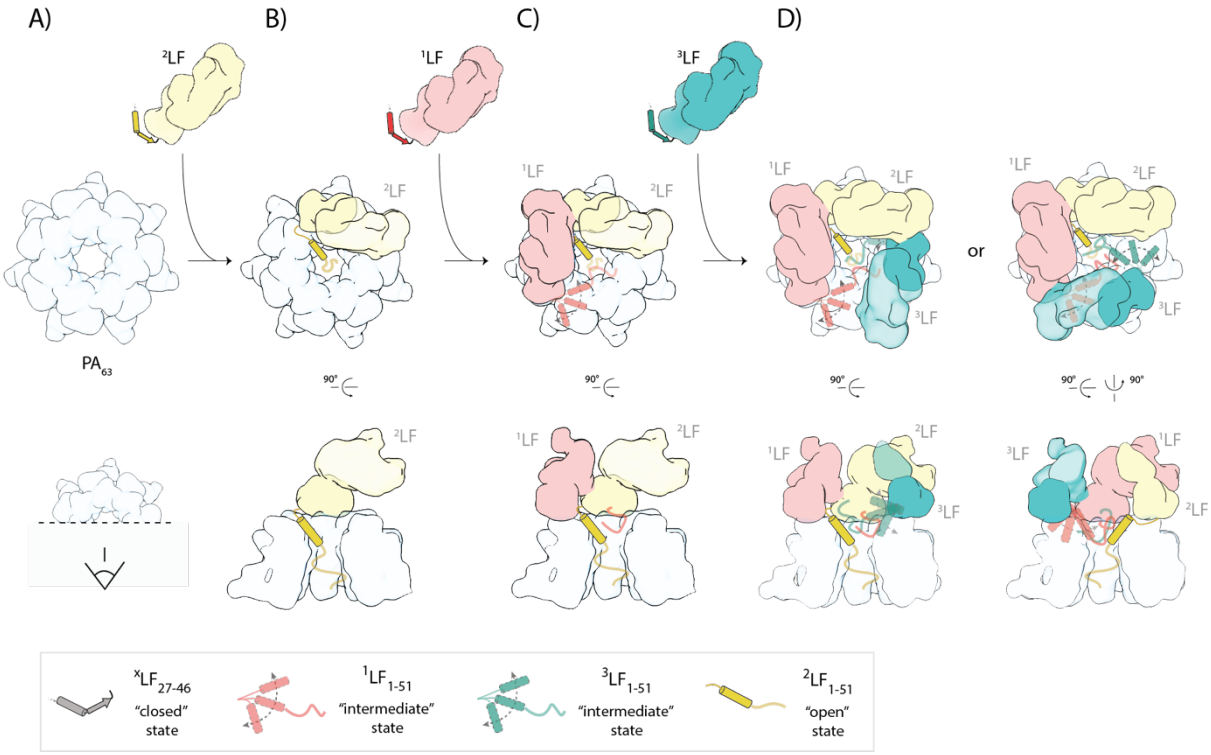

649

650 **Figure 6. Model for PA_7LF_3 assembly.**

651

Supporting information figure captions

Figure S1. Reconstitution of PA_7 into lipid mimetic systems after pore transition.

(**A**) Representative negatively stained electron micrograph areas of PA_7 reconstituted into POPC liposomes (top panels), with individual inserted particles highlighted by white arrowheads. Selection of inserted particles in smaller lipid vesicles (bottom panel). Scale bar: 15 nm. Particles are clearly accumulated at lipid membranes. (**B**) Representative negatively stained electron micrograph area of PA_7 reconstituted in lipid nanodiscs (MSP1D1), with individual inserted particles highlighted by black arrowheads. Scale bar: 20 nm (**C**) Model of PA_7 complexes inserted into lipid nanodiscs with additional examples of individual particles after reconstitution (same nanodiscs as in B). Scale bar: 20 nm.

Figure S2. Purification and cryo-EM of PA_7LF_3.

(**A**) Coomassie-stained SDS-PAGE of purified PA_7LF_3 complex. (**B**) Size exclusion chromatography profile of the PA_7LF_3 complex using a Superdex 200 column. Sample fraction used for cryo-EM studies is indicated by black arrow. (**C**) Representative digital micrograph area of vitrified PA_7LF_3 complex. Scale bar: 20 nm. (**D**) Representative 2-D class averages corresponding to **C**. Scale bar: 10 nm. (**E-H**) Rotated views of the 3-D reconstruction of PA_7LF_{2+1A} (**E**), $PA_7LF_{(2+1A)'}$ (**F**), PA_7LF_{2+1B} (**G**), and $PA_7LF_{3\text{-masked}}$ (**H**), respectively. (**I**) FSC curves between two independently refined half-maps of PA_7LF_{2+1A} (green), $PA_7LF_{(2+1A)'}$ (red), PA_7LF_{2+1B} (blue) and $PA_7LF_{3\text{-masked}}$ (purple).

676 **Figure S3. Flowchart of image processing strategy in SPHIRE.**

677 The single particle processing workflow is shown that included multiple 3-D classification steps
678 as well as rotation of individual classes (indicated by rotation symbol). Number of particles in
679 each class is provided as orange box below the respective structure and the obtained resolution
680 of the map after 3-D refinement is indicated. For each structure a top and side view is shown
681 (in top views PA_7 density is partially clipped to focus on the bound LFs). Mask for masking out
682 third LF is provided in dashed box. Final electron density maps are highlighted by green boxes.
683 Abbreviations: cla3D – 3-D classification, cla2D – 2-D classification, ref-3D – 3-D refinement.
684
685 **Figure S4. Local resolution and 3-D orientation plots.**

686 (**A-D**) Rotated views of the reconstructions, PA_7LF_{2+1A} (**A**), $PA_7LF_{(2+1A)'}$ (**B**), PA_7LF_{2+1B} (**C**),
687 and $PA_7LF_{3\text{-masked}}$ (**D**), respectively, colored by local resolution. Corresponding color key of
688 local resolution is provided on the right. (**E**) Selected examples of side chain densities
689 corresponding to PA and LF with atomic models fitted. (**F**) Rotated views of the 3-D angular
690 distribution plot for the PA_7LF_{2+1A} reconstruction, in which the relative height of bars represents
691 the number of containing particles. Corresponding 2-D histogram is shown on the right. (**G-I**)
692 Same as in **F** for $PA_7LF_{(2+1A)'}$ (**G**), PA_7LF_{2+1B} (**H**), and $PA_7LF_{3\text{-masked}}$ (**I**).
693
694 **Figure S5. Structure comparison of PAs and LFs.**

695 (**A**) Superposition of the seven PA protomers in PA_7LF_3, which are colored in different blue
696 hues (left panel), and a single PA subunit (blue) with the known crystal structure (PDB: 1TZO,
697 green, right panel). Loop region 2β2-2β3 (residues 300-323), resolved only in the crystal
698 structure, is highlighted by a black arrowhead. (**B**) Domain organization of LF with individual
699 domains highlighted by different colors. (**C**) Superposition of individual LFs in the PA_7LF_3
700 structures with ^{1}LF in pink, ^{2}LF in gold, $^{3B}LF_N$ in cyan and $^{3A}LF_N$ in dark green. (**D**)

Superposition of ^{1}LF (pink), ^{2}LF (gold) and unbound LF (PDB: 1J7N, green), aligned via their C-terminal domain. Green and red arrows indicate similar positions in ^{1}LF and unbound LF (PDB:1J7N), respectively. Comparison reveals that the C-terminal domain is rotated respective to the N-terminal domain in the PA_7LF_3 structures. (**E**) Superposition of the N-terminal domain of the three LFs in PA_7LF_3 (green), of LF in the "open" conformation in PA_8LF_4 (PDB: 3KWV, dark yellow) and of unbound LF in the "closed" conformation (PDB: 1J7N, purple). (**F**) Superposition of the three LF-LF interfaces with ^{1}LF-^{2}LF in pink, ^{2}LF-^{3A}LF in green and ^{3B}LF-^{1}LF in blue.

Supporting information movie captions

Movie S1. Conformational change of LF upon PA binding.

The C-terminal domain of the three LF molecules rotate respective to the N-terminal domain upon binding to PA_7 when compared with the unbound LF structure (PDB:1J7N), to form a continuous chain of head-to-tail interactions. Top view of the morph between both conformations is shown, with LFs in blue and PA_7 in transparent grey.

Movie S2. LFs can interact via their C-terminal domains.

In our $PA_7LF_{(2+1A)'}$ reconstruction, two LF molecules interact with each other via their C-terminal domain close to the central axis of the complex, thus forming an additional LF-LF interface. Top view of the morph between this conformation (light blue) and the one observed in the PA_7LF_{2+1A} (yellow) is shown. Volumes are low-pass filtered and shown at the same threshold.

726 **Supporting information table captions**

727

728 **Table S1. Data collection, refinement and model building statistics.**

729

730 **Supporting information figures**

731

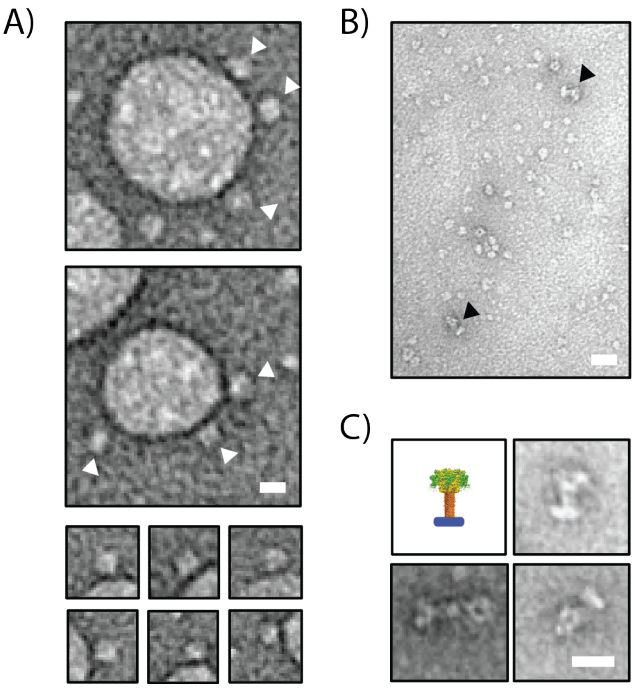

732

733 **Figure S1. Reconstitution of PA_7 into lipid mimetic systems after pore transition.**

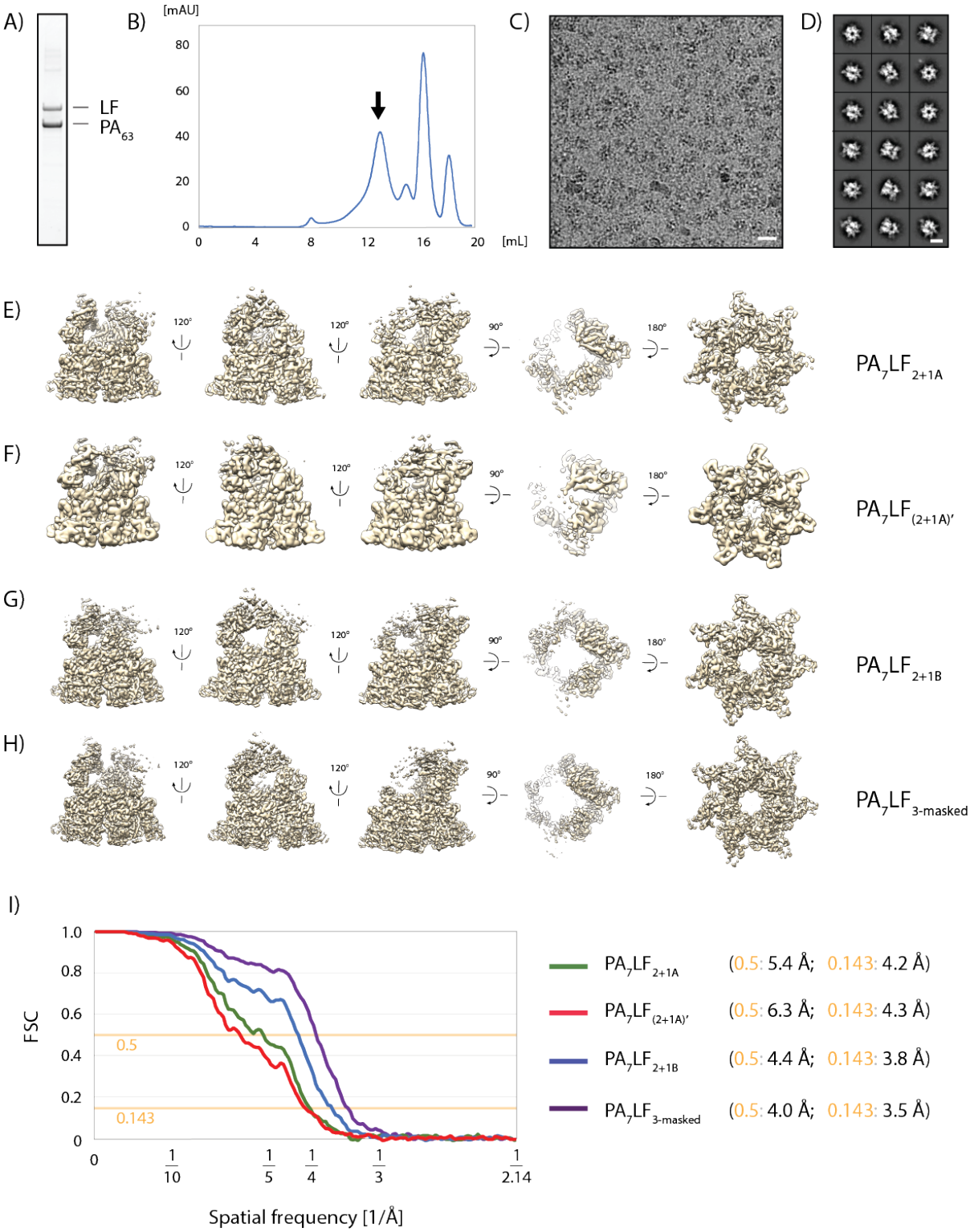

Figure S2. Purification and cryo-EM of PA_7LF_3.

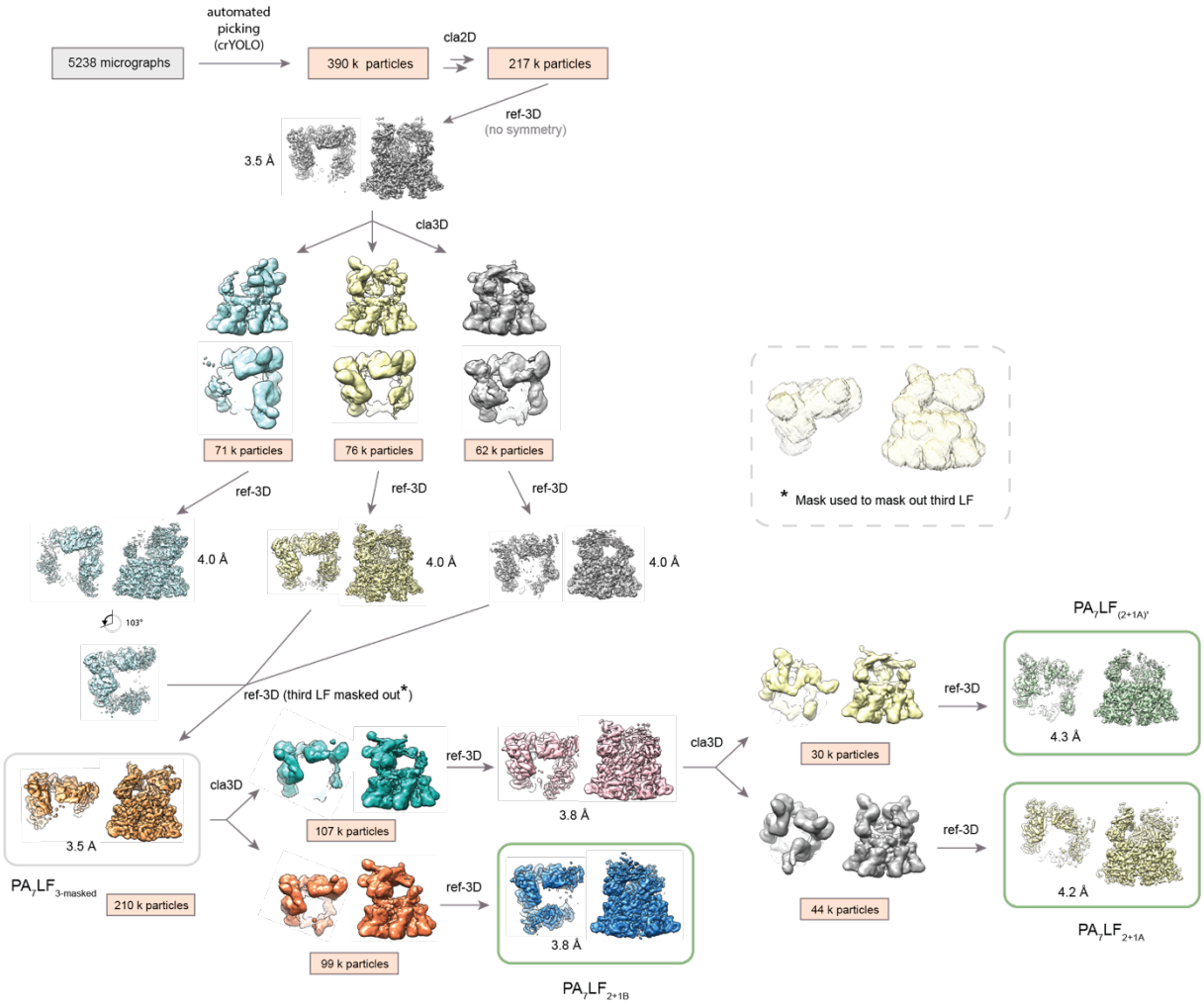

Figure S3. Flowchart of image processing strategy in SPHIRE.

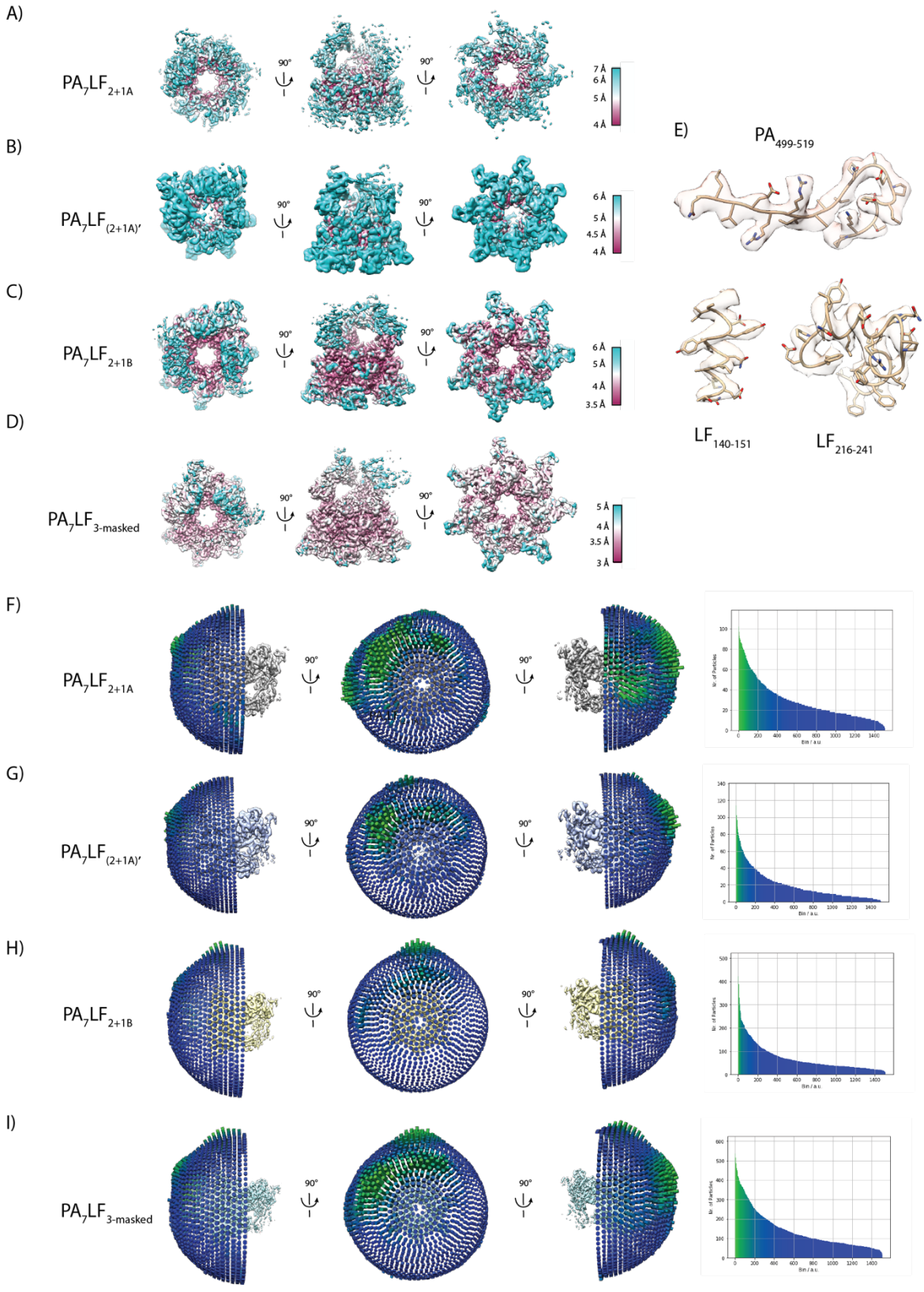

740

741 **Figure S4. Local resolution and 3-D orientation plots.**

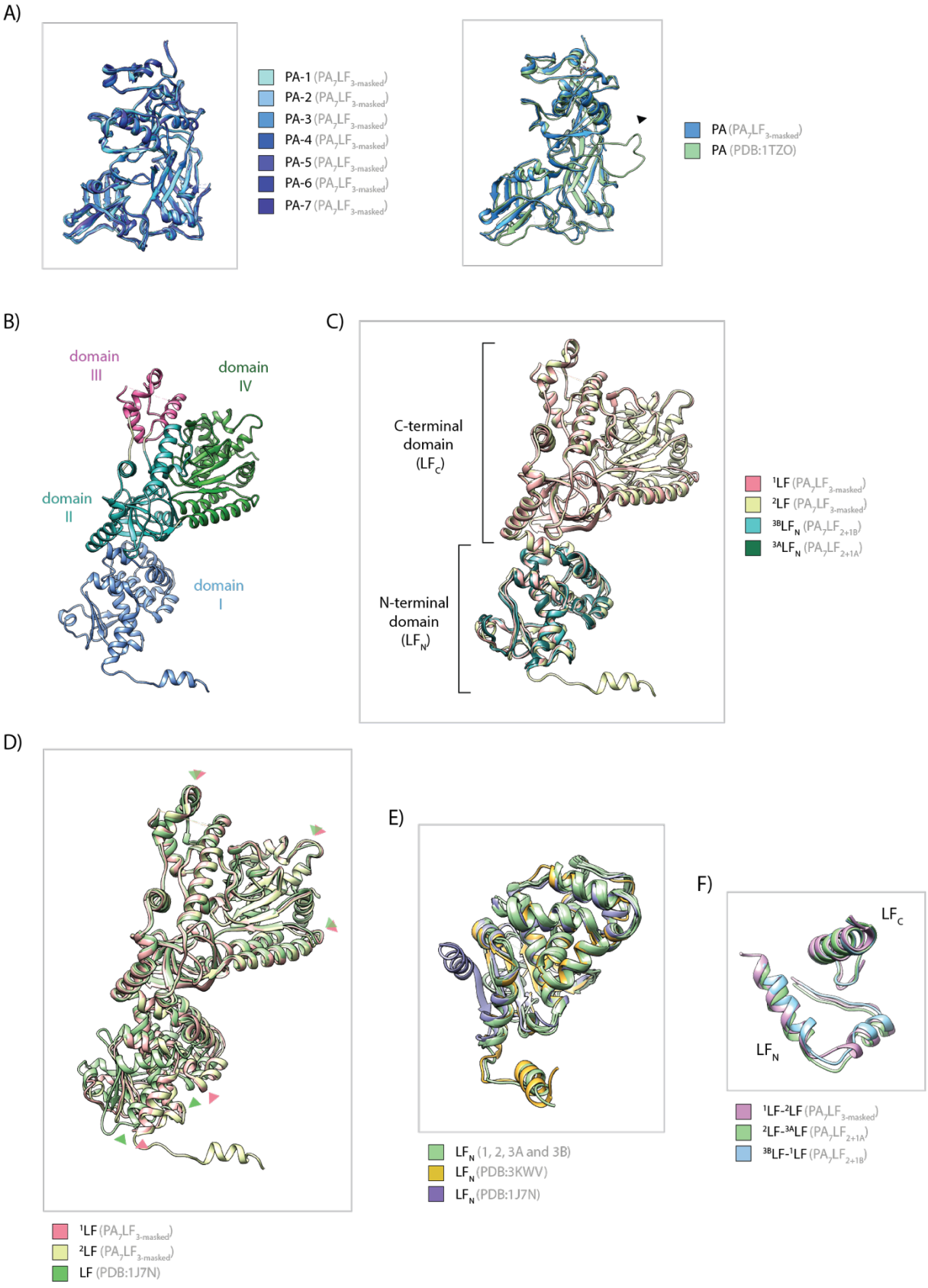

Figure S5. Structure comparison of PAs and LFs.

746 **Supporting information tables**

747

748 **Table S1. Data collection, refinement and model building statistics.**

	$PA_7LF_{3\text{-masked}}$	PA_7LF_{2+1B}	PA_7LF_{2+1A}
Microscopy and cryo-EM			
Microscope	Titan Krios		
Voltage [kV]	300		
Defocus range [μm]	-1.2 to -2.6		
Camera	K2 Summit		
Pixel size [Å]	1.07		
Total electron dose [$e^-/Å^2$]	74.4		
Exposure time [s]	15		
Frames per movie	40		
Number of images	5238		
Map resolution [Å]	3.5	3.8	4.2
Model statistics (phenix)[a]			
Molprobity score	3.00	2.42	
EMRinger	2.34	1.93	
Bond RMSD [Å]	0.008	0.004	
Angle RMSD [°]	0.723	0.753	
Ramachandran favored [%]	90.26	92.10	
Ramachandran outliers [%]	0.03	0.23	
Model statistics (iMODFIT)[a]			
Molprobity score	3.01	2.43	2.63
EMRinger	0.61	0.46	1.18
Bond RMSD [Å]	0.011	0.005	0.009
Angle RMSD [°]	1.201	0.701	0.937
Ramachandran favored [%]	84.37	89.06	86.05
Ramachandran outliers [%]	0.96	0.09	0.02

749

750 [a]A detailed description of which parts of the models were refined with phenix or flexibly fitted using iMODFIT
751 can be found in the Material and Methods section.